nature communications

Article

https://doi.org/10.1038/s41467-025-57278-8

Serum-tolerant polymeric complex for stem-cell transfection and neural differentiation

Received: 12 July 2024

Accepted: 17 February 2025

Published online: 27 February 2025

Check for updates

Yi Jin[1,3], Guochen Han[1,3], Yuemei Gao[1], Hao Cheng[1], Chenhua Sun[1], Jiang Ni[2], Jianping Zhou[1] ✉, Huaqing Zhang[1] ✉ & Yang Ding[1] ✉

Mesenchymal stem cell (MSC) therapy holds promise in biomedical applications but faces challenges in efficient transfection without compromising cell viability. Here, we show a serum-tolerant MSC transfection nanotool, APOs@BP, composed of an apolipoprotein (APO) corona and a boronated polyethyleneimine (BP) core. The APOs corona's serum-protein resistance and cytomembrane affinity enable APOs@BP to achieve 10.4-fold higher transfection efficiency and improved cytocompatibility in serum-containing medium compared to high-molecular-weight polycationic transfectants. For MSC neural differentiation, miRNA-124 and all-trans retinoic acid derivative (atRAN) are further loaded into APOs@BP, forming a polymeric complex for sequential drug release triggered by lysosomal acid and cytosolic reactive oxygen species post-transplantation. Transcriptomic analysis confirms that this system enhances MSC neural differentiation through sequential activation of atRAN-induced differentiation potential and miRNA-124-directed neurogenesis via cGMP-PKG, MAPK, and PI3K-Akt pathways. Transplantation of engineered MSCs reconstructs neural circuits and alleviates cognitive impairment in Alzheimer's disease model mice. Collectively, this system provides a robust and convenient method for MSC-based regenerative medicine.

Regenerative therapies adopting mesenchymal stem cells (MSCs) have shown promise in treating refractory neurological diseases (e.g., Alzheimer's disease (AD)) via neural differentiation and cell replacement to reconstruct the damaged neural circuit[1]. To date, transplantation of MSCs takes unparalleled advantages in cell accessibility and safety over other stem cells (e.g., neural stem cells), but fails to achieve notable clinical benefits for neurodegeneration, as their low spontaneity and uncontrollable directions for MSC differentiation[2].

Neural differentiation of MSCs necessitates a sequential exit from the cell cycle to halt proliferation and initiate differentiation, followed by neuron-specific transcriptional programs under specific signal activation[3]. During this process, the activation of retinoic acid signaling by all-trans retinoic acid (atRA) has been proven as a vital factor in shifting MSCs from self-renewal to a differentiating state[4]. However, atRA-induced stem cells tend to undergo multi-lineage differentiation due to the lack of neural-specific guidance signals[5]. Only a small fraction meets the expectation, necessitating the use of other neurogenic factors to co-regulate differentiation programs more precisely[6]. Among various neurogenesis-related molecules, microRNAs (miRNAs) are key modulators in specific cell fate transitions by simultaneously targeting hundreds of genes and inducing stable epigenetic changes[7]. As the most plentiful miRNA in the nervous system, miRNA-124 (miR-124) is a high-potential driver for the switch of stem cells or somatic cells toward a mature neuronal fate via repressing expression of non-neuronal genes and activating a conserved neural development program[8]. Thus, co-delivering atRA and miR-124 provides a compelling strategy to drive and guide MSC differentiation into neurons.

However, the efficient and safe transfection of MSCs for neural differentiation still faces two main challenges, including inefficient delivery caused by multiple transport barriers, and poor survival due

---

[1]State Key Laboratory of Natural Medicines, Department of Pharmaceutics, China Pharmaceutical University, Nanjing, China. [2]Department of Pharmacy, Affiliated Hospital of Jiangnan University, Wuxi, China. [3]These authors contributed equally: Yi Jin, Guochen Han. ✉e-mail: zhoujianping@cpu.edu.cn; zhanghq0527@163.com; dydszyzf@163.com

to cell susceptibility to culture conditions[9]. Currently, viral vectors and bulk electroporation are the predominant choices for MSC engineering due to their high transfection efficiency[10]. However, their risk of genetic alteration or biological perturbation impels the urgent development of cationic carriers, such as polyethyleneimine (PEI), as safer alternatives[11]. Nevertheless, current protocols for polycationic carriers employ serum-free conditions to prevent transfection failure related to serum instability[12]. However, the absence of serum support or untimely nutrient supplementation, even within a few hours, ruinously disrupts survival, stemness, and post-transfection performance of stem cells due to nutrient depletion. Therefore, there is a pressing need for serum-tolerant transfectants that can efficiently integrate gene and chemical drugs into complexes, and carry them into MSCs without compromising cell viability and differentiation ability.

Upon incubation in serum-containing medium, cationic carrier-drug complexes inevitably absorb serum proteins and form "protein corona" on surface[13]. Protein corona has been demonstrated to confer extrinsic physiochemical properties to complexes and affect their interfacial interactions with environment and cells during transport process[14]. Especially, they would influence biological identity of complexes and determine their kinetic behavior when interacting with cytomembranes[15]. Among corona proteins, apolipoproteins (APOs) with high abundance ($> 20\%$) are the only lipophilic protein capable of facilitating particle incorporation into cytomembranes through the insertion of amphiphilic alpha (α)-helices into lipid bilayer, implying potential for transmembrane delivery of drugs[16]. Therefore, we hypothesize that employing APOs surface-decoration strategy might create steric hindrance against external serum proteins and enhance on-membrane interactions to improve complex stabilization and transfection efficiency for MSC engineering.

In this work, we devise a serum-tolerant strategy by decorating cationic polymer complexes with APOs to mitigate serum-protein interference and enhance cytomembrane interactions, facilitating efficient MSC transfection under serum-containing conditions. To activate neural differentiation potential of MSCs, polymeric complexes are synthesized by integrating all-trans retinoic acid aminated derivative (atRAN) and miR-124 into boronated polyethyleneimine (BP) core (APOs@^{atRAN}BP$_{miR\text{-}124}$) via coordination binding and electrostatic compression, respectively (Fig. 1a). The application of APOs@^{atRAN}BP$_{miR\text{-}124}$ involves three steps in MSC engineering for AD treatment, as described below. (i) A serum-tolerant APOs shell prevents serum-protein adsorption by steric hindrance and promotes on-membrane interaction to facilitate MSC transfection. Upon internalization, atRAN release triggered by lysosomal acid in engineered MSCs (eMSCs) activates MSC differentiation potential via retinoic acid signaling pathway. (ii) eMSCs are then transplanted into AD model mice via stereotactic injection into hippocampus. (iii) Triggered by the elevated cytosolic reactive oxygen species (ROS) post-transplantation, miR-124 is liberated from degraded BP polymeric core, directing neural differentiation through cGMP-PKG, MAPK, and PI3K-Akt signaling pathways, thereby restoring neural network (Fig. 1b). This system provides a robust and convenient approach for highly efficient and safe MSC transfection, enabling precise control over MSC neural differentiation for treating neurodegenerative diseases, especially AD.

Results

APOs decorated complexes for MSC transfection and engineering

MSC engineering has advanced cell replacement therapies for refractory diseases by introducing exogenous agents (e.g., gene and chemical drugs) to control differentiation. However, differentiation regulation faces challenges in low spontaneity and unpredictable differentiation directions. As a result, there remains a demand for safe and efficient engineering tools to integrate multiple regulators and overcome transfection barriers without compromising cell viability.

Owing to low-toxicity and modifiability, polyethylenimine with low molecular weight of 10 kDa (^{10K}PEI) was employed and further modified with phenylboronic acid (PBA) to increase the positive charge for gene compression and provide loading site for small molecules (Supplementary Fig. 1). To overcome serum-protein absorption during MSC transfection, we further introduced surface-modified apolipoproteins (APOs) to enhance serum tolerance and cytomembrane-affinity interaction, thereby improving the transfection efficiency of the boronated PEI polymer (BP). As shown in Supplementary Fig. 2, the chemical structure of BP polymers with a 31.5% degree of substitution was confirmed using ^{1}H NMR, as evidenced by the peaks at 7.0-8.0 ppm that were assigned to a benzene ring, and peaks at 2.5-3.5 ppm that assigned to adjacent methyl groups linked to quaternary ammonium moiety, respectively. Moreover, the molecular mass of BP was determined to be 22 kDa (Supplementary Fig. 3). After simple mixing, BP polymers effectively condensed miRNA through electrostatic interactions to form BP$_{miRNA}$ complex. Subsequently, APOs were decorated onto these complexes via simple incubation to create APOs-modified polymeric complexes (APOs@BP$_{miRNA}$). APOs@BP$_{miRNA}$ exhibited a shell-core structure with an increased particle size of approximately 107 nm and a reduced zeta potential of 15.7 mV compared to bare BP$_{miRNA}$, indicating the successful surface assembly of negatively charged APOs (Supplementary Fig. 4). To compare miRNA compression capability of different PEI derivatives, a gel electrophoresis assay was performed with different N/P ratio. As illustrated in Supplementary Fig. 5, APOs@BP with quaternary ammonium exhibited a remarkably lower N/P ratio of 1 compared to ^{10K}PEI (N/P ratio of 2.5) and PEI with higher molecular weight of 25 kDa (^{25K}PEI, N/P ratio of 2), confirming superior miRNA loading efficiency of APOs@BP. Moreover, APOs@BP transfection ability was further assessed in MSCs. The MSCs isolated from umbilical cord tissue were confirmed for purity and phenotype by positive expression of CD44, CD90, and CD105, negative expression of CD34 and CD45, and typical fusiform morphology (Supplementary Figs. 6 and 7).

Thereafter, we investigated both transfection efficacy and cytocompatibility of different polymeric complexes in serum-free and 10% fetal bovine serum (FBS)-containing medium. FAM-labeled miRNA (FAM-miRNA) was utilized to visually compare miRNA transfection efficiency; ^{10K}PEI and ^{25K}PEI were set as controls for miRNA compression to form ^{25K}PEI$_{FAM\text{-}miRNA}$ and ^{10K}PEI$_{FAM\text{-}miRNA}$, respectively. As shown in Fig. 2a, the transfection efficiency of BP$_{FAM\text{-}miRNA}$ without APOs modification was high in absence of 10% FBS but sharply diminished in the presence of 10% FBS; groups of ^{25K}PEI$_{FAM\text{-}miRNA}$ and ^{10K}PEI$_{FAM\text{-}miRNA}$ also gave a noticeable decrease of transfection efficiency. In contrast, APOs@BP$_{FAM\text{-}miRNA}$ barely changed in transfection efficacy even in the presence of serum, with ~73.9% of positive cell percentage and miRNA delivery efficiency that was 7.5-, 10.4-, and 13.6-fold higher than that of BP$_{FAM\text{-}miRNA}$, ^{25K}PEI$_{FAM\text{-}miRNA}$ and ^{10K}PEI$_{FAM\text{-}miRNA}$, respectively (Supplementary Figs. 8 and 9). Collectively, only APOs@BP accomplishes efficient serum-tolerant transfection in MSCs, meeting the essential need for serum during the transfection process.

Cytocompatibility is another critical concern during transfection, particularly for sensitive cell populations such as MSCs. As shown in Fig. 2b, MSCs exhibited approximately 14.4% higher survival rates when transfected in the presence of serum as opposed to serum-absent conditions. Even in the presence of trophic factors from serum, ^{25K}PEI displayed serious cytotoxicity (only 60.4% of cell viability) and hindered MSC proliferation (Fig. 2c). Commendably, ^{10K}PEI, BP and APOs@BP all shared low cytotoxicity ($> 90.0\%$ of cell viability) in MSC culture. Taken together, these results suggest that APOs@BP serves as an efficient and biocompatible transfection tool for MSC engineering in serum-containing medium.

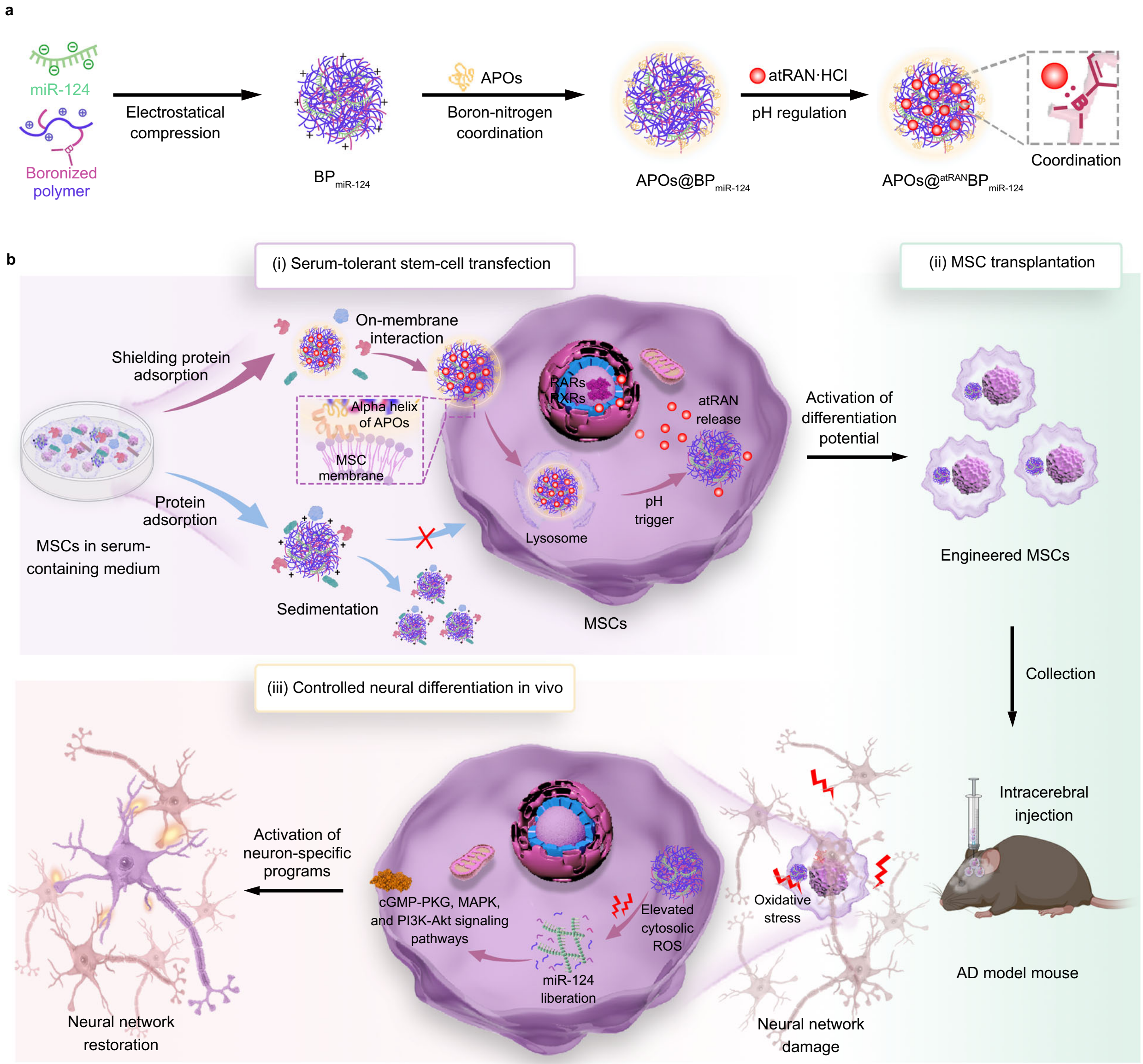

Fig. 1 | Schematic diagram of preparation and therapeutic mechanism of APOs@^{atRAN}BP$_{miR\text{-}124}$-enginneered MSCs (APOs@^{atRAN}BP$_{miR\text{-}124}$-eMSCs) for AD treatment. a For preparation, miR-124, APOs, and atRAN were integrated into BP to prepare APOs@^{atRAN}BP$_{miR\text{-}124}$ through electrostatic binding and boron-nitrogen coordination. **b** The APO corona shells prevented serum-protein adsorption and enhanced complex-cytomembrane interaction to control neuronal differentiation of eMSCs. During this process, atRAN release triggered by lysosomal acid activated MSC differentiation potential. Following stereotactic injection into hippocampus of AD model mice, miR-124 release was triggered by intracerebral ROS accumulation. eMSCs then underwent neuronal differentiation mediated by miR-124-induced neuron-specific programming activation, resulting in neural circuit reconstruction[26].

Mechanisms of serum defense for high transfection via APOs surface-decoration

The efficient MSC transfection encounters multiple barriers, starting with serum stability, cellular endocytosis, lysosomal escape, and ultimately gene release, which collectively determine transfection efficacy. Hence, these factors were investigated to elucidate the underlying mechanisms behind the high transfection efficiency of APOs@BP. The biostability against serum-protein adsorption is of great importance to promote membrane interaction and cytosolic delivery of cargoes into MSCs. To assess the impact of APOs on serum stability, polymeric complexes were exposed to medium containing 10% FBS, and subsequently collected through centrifugation. Transmission electron microscopy (TEM) and dynamic light scattering (DLS) analysis revealed that groups absent of APOs decoration including BP$_{miRNA}$, ^{10K}PEI$_{miRNA}$ and ^{25K}PEI$_{miRNA}$, experienced rapid aggregation, resulting in at least 4.2-fold increase in particle size within half an hour upon exposure to serum (Fig. 2d, e). In contrast, APOs@BP$_{miRNA}$ maintained a monodisperse and uniform size distribution. Thereafter, serum-protein adsorption was measured using polyacrylamide gel electrophoresis (PAGE) and bicinchoninic acid (BCA) assay. As shown in Fig. 2f and Supplementary Fig. 10, BP$_{miRNA}$ aggravated serum-protein adsorption through nitrogen-boron complexation between PBA and proteins, which elucidated why there was a dramatic reversal in transfection efficiency of BP in serum conditions. In contrast, the APOs decoration protected polymeric complexes from serum-protein attack with 57.0% reduction in amounts of adsorbed proteins, resulting in desirable biostability of APOs@BP$_{miRNA}$. These findings suggest that serum-protein resistance of APOs layer confers stability to APOs@BP$_{miRNA}$, and consequently facilitates high efficiency of miRNA transfection in a serum-containing medium (Fig. 2g).

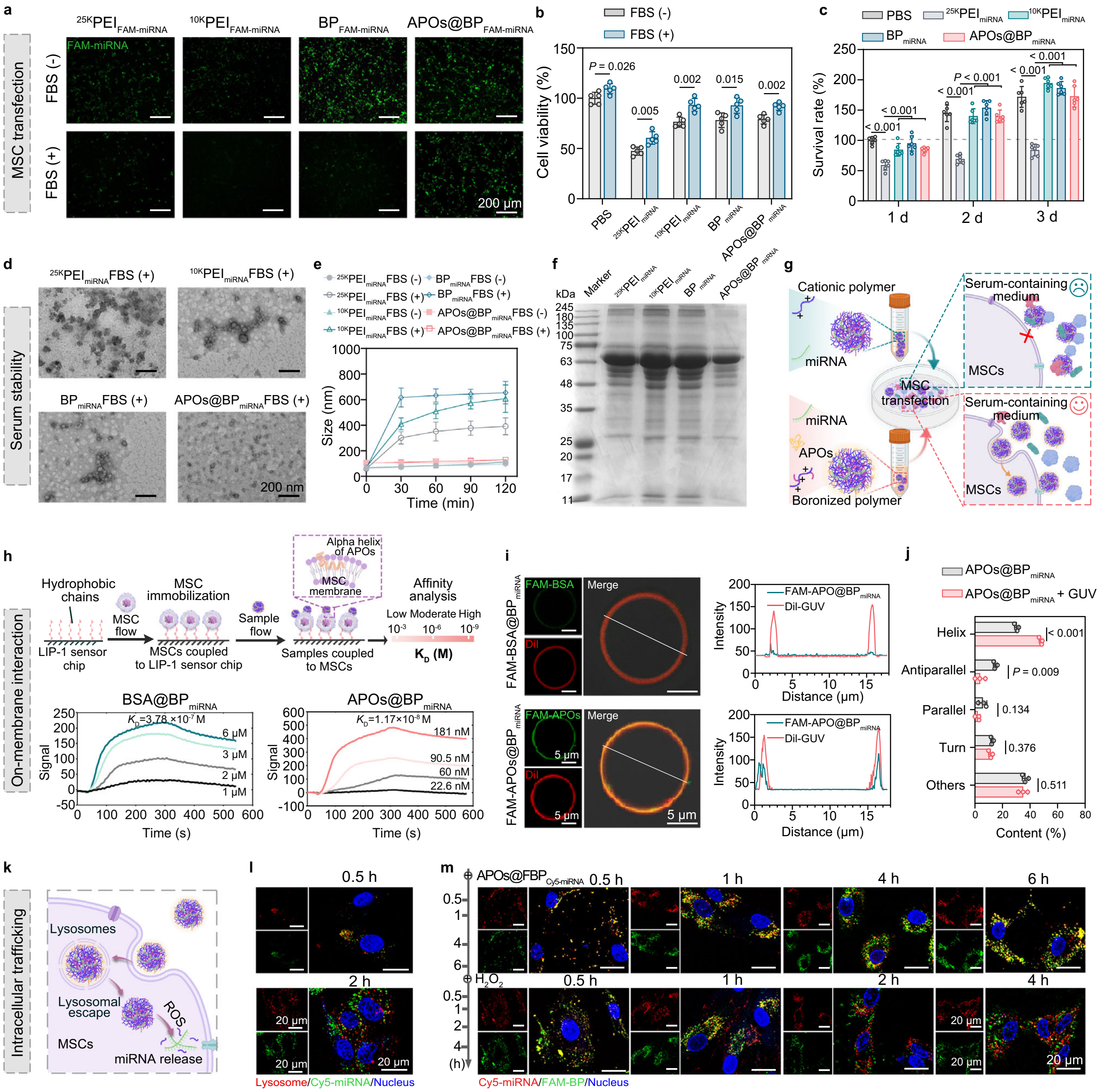

Fig. 2 | Transfection efficiency and mechanisms of APOs@BP in MSCs in serum-containing medium. a Representative fluorescent images of MSCs after FAM-miRNA (green) transfection with ^{25K}PEI$_{\text{FAM-miRNA}}$, ^{10K}PEI$_{\text{FAM-miRNA}}$, BP$_{\text{FAM-miRNA}}$, and APOs@BP$_{\text{FAM-miRNA}}$ in medium with or without 10% FBS. **b** Cell viability after transfection with ^{25K}PEI$_{\text{miRNA}}$, ^{10K}PEI$_{\text{miRNA}}$, BP$_{\text{miRNA}}$, and APOs@BP$_{\text{miRNA}}$ in medium with or without 10% FBS. **c** Cell proliferation in 3 days after transfection with ^{25K}PEI$_{\text{miRNA}}$, ^{10K}PEI$_{\text{miRNA}}$, BP$_{\text{miRNA}}$, and APOs@BP$_{\text{miRNA}}$ in medium with 10% FBS. **d** Representative TEM images of ^{25K}PEI$_{\text{miRNA}}$, ^{10K}PEI$_{\text{miRNA}}$, BP$_{\text{miRNA}}$, and APOs@BP$_{\text{miRNA}}$ after incubation in 10% FBS for 2 h. **e** Evaluation of the stability of ^{25K}PEI$_{\text{miRNA}}$, ^{10K}PEI$_{\text{miRNA}}$, BP$_{\text{miRNA}}$, and APOs@BP$_{\text{miRNA}}$ in the presence or absence of serum by measuring particle size, respectively. **f** Determination of protein adsorption of polymeric complexes by SDS-PAGE. **g** Schematic illustration of serum-tolerant polymeric complexes to avoid serum-protein adsorption[27]. **h** SPR analysis of MSC membrane binding affinity of BSA@BP$_{\text{miRNA}}$ and APOs@BP$_{\text{miRNA}}$[28] **i** CLSM images of lipid vesicles (labeled with DiI, red) after incubation with FAM labeled BSA@BP$_{\text{miRNA}}$ and APOs@BP$_{\text{miRNA}}$ (green), respectively. The solid white line denotes the straight-line distance employed for colocation analysis between DiI and FAM signals on the right. **j** The conformational content of APOs in APOs@BP$_{\text{miRNA}}$ before and after incubation with lipid vesicles. **k** Schematic illustration of intracellular trafficking of APOs@BP$_{\text{miRNA}}$[29]. **l** The dynamic colocalization of APOs@BP$_{\text{Cy5-miRNA}}$ (green) and lysosomes (red) in MSCs after incubation for 0.5 and 2 h, respectively. **m** Intracellular accumulation and ROS-triggered dissociation of Cy5-miRNA (red) from polymerized carrier (FBP, green). Data were presented as mean ± SD ($n = 5$ independent samples in **b**; $n = 6$ independent samples in **c**; $n = 3$ independent samples in **e**, **j**;). Two-tailed unpaired t-test was used for statistical analysis of **b**, **j**. One-way ANOVA with Dunnett's multiple comparisons test was used for statistical analysis of **c**. Three independent experiments were performed with similar results and representative results are shown. Source data are provided as a Source Data file.

Serum-protein coronas redefine extrinsic physiochemical properties of polymeric complexes and promote cytomembrane interaction for transmembrane transport of drugs[17]. Characterized by abundant amphiphilic helical domains, APOs exhibit inherent affinity for membrane contacting, enabling positive cellular interaction through hydrophobic insertion that differs from other serum-proteins (e.g., serum albumin)[18,19]. In this study, the dynamic membrane-binding behaviors of different protein modified BP$_{\text{miRNA}}$ on MSCs were monitored using surface plasmon resonance (SPR) analysis. Living MSCs were immobilized onto a LIP-1 sensor chip via hydrophobic interactions, and binding affinity constant (K_D) was calculated using a 1:1 Langmuir binding model (Fig. 2h). Bovine serum albumin (BSA) surface-decoration of BP_{miRNA} ($BSA@BP_{miRNA}$) served as control. As shown in Fig. 2h, Supplementary Fig. 11 and Supplementary Table 1, in contrast to free BSA demonstrating a moderate membrane-binding affinity with K_D value of 4.8×10^{-6} M, amphiphilic APOs revealed an impressive 293.2-fold higher binding affinity ($K_D = 1.6\times 10^{-8}$ M), attributed to the abundance of lipid-binding motif within APOs. The presence of APOs endowed $APOs@BP_{miRNA}$ with comparable membrane-binding affinity ($K_D = 1.2 \times 10^{-8}$ M), which was approximately 32-fold higher affinity than $BSA@BP_{miRNA}$ ($K_D = 3.8 \times 10^{-7}$ M), highlighting complex-membrane interaction from APOs (Supplementary Fig. 12).

To further visualize the interaction with lipid membranes, APOs and BSA were labeled with FAM for on-membrane tracking. The polymeric complexes (labeled with FAM, in green) were co-incubated with giant unilamellar vesicles (GUVs) labeled with DiI (a lipophilic dye in red). Compared to $FAM\text{-}BSA@BP_{miRNA}$, $FAM\text{-}APOs@BP_{miRNA}$ group appeared more effective in binding with GUVs, as evidenced by the obvious co-localized fluorescence signal on the membrane (Fig. 2i). Lipid binding of APOs has been proved to trigger a conformational transition of APOs from a random coil to α-helix, leading to an augmentation in helicity[20]. Hence, circular dichroism (CD) spectra analysis revealed that helix content of APOs in complexes increased from 30.4% to 48.0%, while antiparallel content decreased from 14.8% to 3.7% (Supplementary Fig. 13 and Fig. 2j), indicating a conformational change of APOs characterized by enhanced hydrophobicity after lipid binding. Consequently, on-membrane interaction of $APOs@BP_{miRNA}$ experienced 2.2-fold increase in cellular uptake efficiency in the serum-containing medium compared to $BSA@BP_{miRNA}$ (Supplementary Fig. 14). Collectively, these results indicate that APOs decoration enhances serum stability of polymeric complexes and enables their insertion into cytomembrane, thereby facilitating drug transport into MSCs under serum conditions.

After cellular internalization, $APOs@BP_{miRNA}$ underwent temporal intracellular trafficking events including endo/lysosomal escape and miRNA discharge (Fig. 2k). As observed by confocal laser scanning microscopy (CLSM), $APOs@BP_{Cy5\text{-}miRNA}$ (in green) rapidly escaped from lysosomes (in red) and distributed evenly within cells in 2 h, as evidenced by disappearance of yellow dots and appearance of green dots in the cytoplasm (Fig. 2l). The efficient endosomal escape of $APOs@BP_{miRNA}$ was attributed to pH buffering effect of PEI backbone, together with the absorption of lysosomal membrane proteins by PBA moieties after pH-responsive detachment of APOs shell[21]. After the lysosomal escape, intracellular dissociation of miRNA from the carrier is the final crucial step for miRNA delivery. As presented in Fig. 2m, yellow fluorescence signal that implied co-localization of red Cy5-miRNA and green FAM-BP (FBP) was existed even after 6 h of incubation, revealing minimal miRNA release from $APOs@BP_{Cy5\text{-}miRNA}$ under normal conditions. However, $APOs@BP_{Cy5\text{-}miRNA}$ displayed rapid miRNA release upon exposure to H_2O_2 (0.1 mM), which simulated pathological signals of reactive oxygen species (ROS) at the AD lesion sites, and infiltrated into MSCs (Supplementary Fig. 15). ROS-triggered miRNA release behavior was attributed to the cleavable side chain of BP polymer, which underwent oxidation reaction of carbon-boron bond and subsequent hydrolysis, leading to charge reversal for miRNA release (Supplementary Fig. 16). Thereafter, gel retardation electrophoresis was employed to investigate ROS-responsive miRNA release from $APOs@BP_{miRNA}$. Specifically, 0.001 mM of H_2O_2 was utilized to simulate a normal physiological environment within MSC cytoplasm, while 0.1 and 1.0 mM of H_2O_2 represented ROS accumulation at the lesion site. As a control, nonresponsive PBA-modified PEI polymer (NP) was synthesized and formulated into $APOs@NP_{miRNA}$ (Supplementary Figs. 17 and 18). Gel electrophoresis analysis in Supplementary Fig. 19 indicated ignorable gene release from $APOs@NP_{miRNA}$, even at high H_2O_2 concentrations. When exposed to 0.001 mM of H_2O_2, the ignorable miRNA release was observed, demonstrating the failure of miRNA release from $APOs@BP_{miRNA}$ in MSC cytoplasm. In contrast, miRNA release was observed from $APOs@BP_{miRNA}$ upon exposure to 0.1 mM H_2O_2, providing the possibility of ROS-responsive miRNA release for MSC engineering in AD lesion sites. These results indicate that $APOs@BP_{miRNA}$ shares multi-capabilities, including serum tolerance, enhanced membrane interaction, highly efficient cellular internalization, rapid endo/lysosomal escape, and ROS-responsive miRNA release for MSC transfection and engineering therapy.

pH/ROS sequential-responsive release of atRAN and miR-124 after transfection

In addition to highly efficient gene transfection, APOs@BP possessed abundant PBA groups that could coordinate to nitrogen-containing chemicals. Specifically, chemicals with poor solubility can be modified into salts to avoid the use of organic solvents in MSC engineering and thus ensure cell viability. This property of APOs@BP favored the co-delivery of different agents to regulate intricate cellular processes like MSC differentiation. To control neural differentiation of MSCs, it involves two stages of withdrawal from cell proliferation into differentiation priming state, and subsequent activation of neuron-specific genetic programs. Therefore, two agents of atRA and miR-124 that can activate differentiation potential and neural development programs were employed to direct neural differentiation[22,23]. For intracellular delivery, a nitrogen-containing atRA derivative (atRAN) was synthesized and expected to be co-integrated with miR-124 into APOs@BP via boron-nitrogen coordination and electrostatic compression, respectively. The atRAN preserved the critical binding domains for effective interaction with retinoic acid receptors (RARs) (Supplementary Fig. 20a). Consequently, it exhibited comparable abilities to atRA in inducing downstream signaling molecules (Wnt2b and NeuronD1) essential for neural differentiation (Supplementary Fig. 20b)[24]. To overcome atRAN insolubility for coordination loading in mild conditions, a hydrochloride form with increased polarity and high solubility (1765 μg mL^{-1}) was further synthesized and confirmed, which could be desalted to atRAN under weak alkaline conditions for coordination loading (Supplementary Fig. 20c–g and Supplementary Table 2), while also avoiding the use of organic solvents to maintain cell viability during MSC transfection[22,23]. Subsequently, atRAN was simply encapsulated into $APOs@BP_{miR\text{-}124}$ by incubation in PBS solution (pH 8.5) to form $APOs@^{atRAN}BP_{miR\text{-}124}$, offering particle size of ~109 nm, atRAN entrapment efficiency of (85.31 ± 0.54)% and drug loading of (5.75 ± 0.04)%, and a similar shell-core structure as $APOs@BP_{miR\text{-}124}$ (Fig. 2a). In X-ray photoelectron spectroscopy (XPS) analysis of B *1s* spectra, in comparison to physical mixture (at 191.4 eV), negatively shifted peaks in $^{atRAN}BP_{miR\text{-}124}$ (at 188.0 eV) and $APOs@^{atRAN}BP_{miR\text{-}124}$ (at 187.8 eV) were observed (Fig. 3b and Supplementary Fig. 21), indicating that atRAN and APOs formed boron-nitrogen coordination with PBA moieties of $BP_{miR\text{-}124}$.

The PBA moieties and cleavable side chains in BP polymer allowed for pH-responsive chemical release and ROS-responsive gene release, respectively. Considering that intracellular $APOs@^{atRAN}BP_{miR\text{-}124}$ successively escaped from acidic lysosomes (low pH) during transfection and then entered the ROS-infiltrated cytoplasm (high ROS) after MSC transplantation into the lesions, we attempted to harness this process for sequentially triggered discharge of atRAN and miR-124. To verify the hypothesis, release profiles of atRAN and miR-124 from $APOs@^{atRAN}BP_{miR\text{-}124}$ were assessed in PBS solutions with different pH values and H_2O_2 concentrations to simulate different physiological conditions. These conditions included pH 7.4 (the culture medium), pH 5.0 (lysosomes), pH 5.0 in the presence of 0.1 mM H_2O_2 (the ROS-rich lysosomes after MSC implantation), pH 7.4 in the presence of

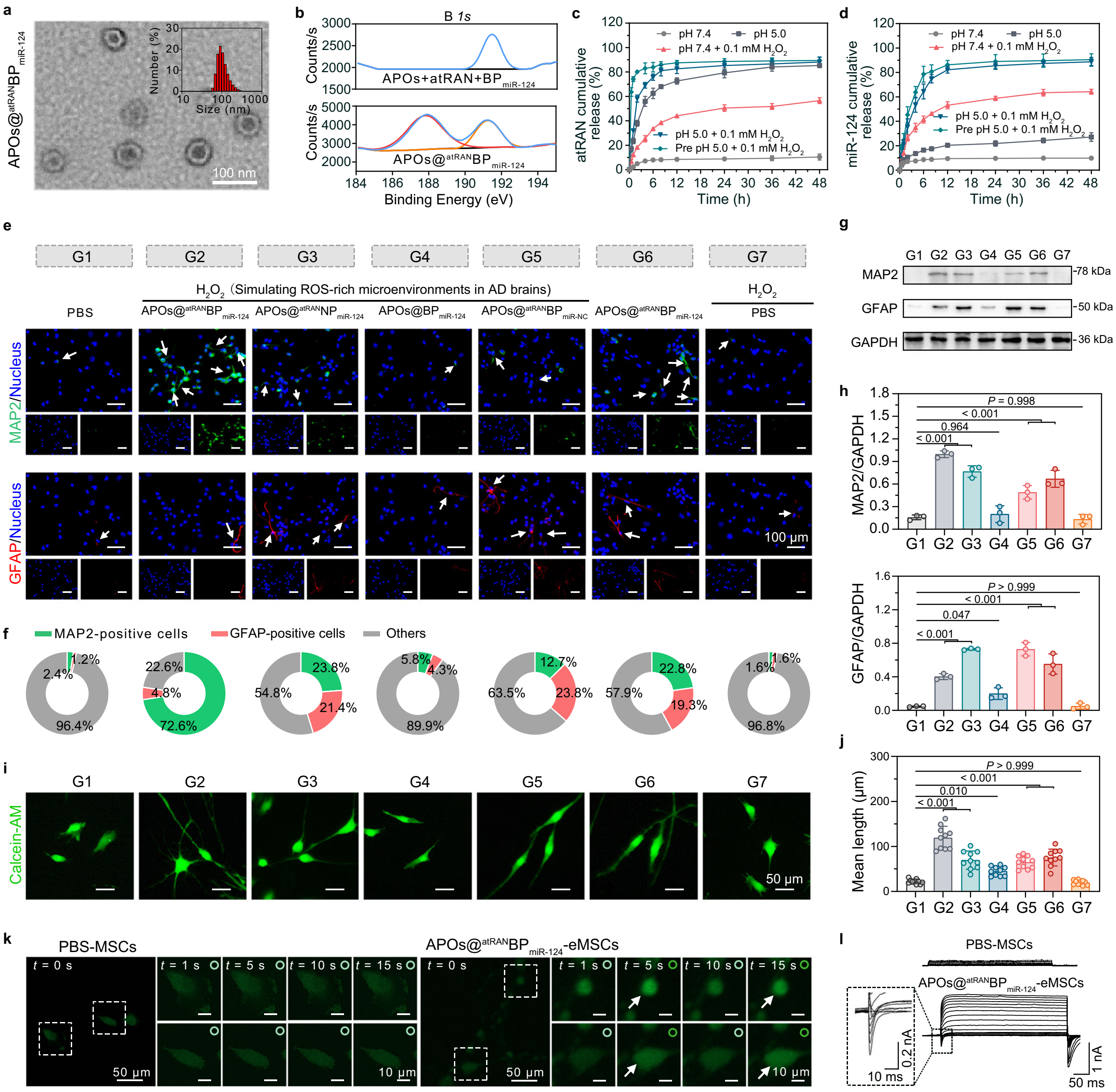

Fig. 3 | Neural differentiation of MSCs directed by APOs@$^{\text{atRAN}}$BP$_{\text{miR-124}}$. **a** The morphology and size distribution of APOs@$^{\text{atRAN}}$BP$_{\text{miR-124}}$. **b** B *1s* spectra of APOs@$^{\text{atRAN}}$BP$_{\text{miR-124}}$ and physical mixture of APOs, atRAN, and BP$_{\text{miR-124}}$ measured by XPS. **c** In vitro release behavior of atRAN from APOs@$^{\text{atRAN}}$BP$_{\text{miR-124}}$ at different conditions. The media conditions of pH 7.4 and 5.0 simulated culture medium and lysosomes of MSCs, respectively, while the medium of pH 5.0 or pH 7.4 in the presence of 0.1 mM H_2O_2 simulated ROS-rich lysosomes and cytoplasm after MSC transplantation into AD lesion sites, respectively. 0.1 mM of H_2O_2 pre-treatment at pH 5.0 for 6 h simulated ROS-rich cytoplasm post-escape from lysosomes. **d** In vitro release behavior of miR-124 from APOs@$^{\text{atRAN}}$BP$_{\text{miR-124}}$ at different media conditions as described above. **e** Immunofluorescence analysis of eMSCs in different groups. MAP2 (green) immunostaining for neurons. GFAP (red) immunostaining for astrocytes. The white arrows indicate positive cells. **f** Quantification of the proportions of GFAP-positive and MAP2-positive cells. **g** Western blot assay of the expression of GFAP and MAP2 in eMSCs. **h** Quantification of data from (**g**). **i** Morphology of eMSCs (labeled with calcein-AM, green) in different groups. **j** Mean lengths of neurites in eMSCs of different groups. **k** Ca^{2+} images of Fluo-4 AM-labeled PBS-MSCs (green) and APOs@$^{\text{atRAN}}$BP$_{\text{miR-124}}$-eMSCs (green) after addition of physiological buffers containing 50 mM KCl, respectively. The white dashed box indicates the magnified region, and white arrows indicate changes in cell fluorescence. The green hollow circles indicate cell fluorescence intensity. **l** Representative voltage-dependent membrane currents of PBS-MSCs and APOs@$^{\text{atRAN}}$BP$_{\text{miR-124}}$-eMSCs. The black dashed box indicates the magnified region. Data were presented as mean ± SD ($n = 3$ independent samples in **c**, **d**, **h**; $n = 10$ independent cell samples in **j**). One-way ANOVA with Dunnett's multiple comparisons test was used for statistical analysis of **h**, **j**. Three independent experiments were performed with similar results and representative results are shown. Source data are provided as a Source Data file.

0.1 mM H_2O_2 (the ROS-rich cytoplasm after MSC implantation), and 0.1 mM H_2O_2 with pre-treating at pH 5.0 for 6 h (ROS-rich cytoplasm post-escape from lysosomes). As shown in Fig. 3c, negligible atRAN released from APOs@$^{\text{atRAN}}$BP$_{\text{miR-124}}$ was observed at pH 7.4, indicating stability in culture medium. In the presence of H_2O_2 at pH 7.4, the release percentage of atRAN increased due to the ROS-triggered cleavage of side chains on BP. In contrast, atRAN was released rapidly at pH 5.0, which was up to 72.7% within 12 h, attributed to the pH-responsive breakage of the coordination bond between atRAN and PBA.

As presented in Fig. 3d, only a modest release profile of miR-124 (9.8%) from APOs@^{atRAN}BP$_{miR\text{-}124}$ was observed within 48 h at pH 7.4, indicating no significant miR-124 burst release in the culture medium. Upon detachment of the APOs shell and atRAN at pH 5.0, the release percentage of miR-124 gave a slight increase to 27.1%, due to the loosening of polymeric complex structure. In contrast, H_2O_2-contained media at pH 5.0 resulted in a rapid release of miR-124 with the release percentage reaching up to 88.8%, which was attributed to ROS-triggered oxidation and degradation of BP. Accordingly, a pH/ROS sequential-responsive drug release behavior is favorable for programmed activation of atRAN-increased differentiation potential and miR-124-directed neurogenesis, allowing for precise control over differentiation of MSCs into neurons in lesion sites.

Directed differentiation into neurons from engineered MSCs

During differentiation towards neurons, MSCs undergo various alterations, including expression of neuron-specific markers, elongation of neurites, and maturation of electrophysiological functions. Hence, these aforementioned factors were investigated to assess whether APOs@^{atRAN}BP$_{miR\text{-}124}$ could guide the neural differentiation of MSCs. Immunostaining was performed for assessing the expression of microtubule-associated protein 2 (MAP2, a tubulin marker of neurons) and glial fibrillary acid protein (GFAP, a protein mainly distributed in astrocytes) in engineered MSCs (eMSCs) cultured for 30 days. To simulate ROS-rich microenvironment in AD lesion sites, a culture medium containing H_2O_2 (0.1 mM) was applied to induce an increased intracellular ROS level in eMSCs. As shown in Fig. 3e, f, MSCs gave no spontaneous tendency to differentiate into neurons (MAP2 positive cells, in green) or astrocytes (GFAP positive cells, in red) after 30-day culture with or without H_2O_2 pretreatment, indicating negligible influence of ROS on the neural differentiation of MSCs. After polymeric complex treatment, we observed red (GFAP) and green (MAP2) signals that indicated the occurrence of MSC differentiation. Compared to APOs@BP$_{miR\text{-}124}$ group, APOs@^{atRAN}BP$_{miR\text{-}NC}$ treatment provided 2.2-fold higher neural differentiation efficiency of 12.7% (MAP2-positive cells/DAPI-positive cells), but led to improved glial differentiation efficiency of 23.8% (GFAP-positive cells/DAPI-positive cells) due to non-specific differentiation activation of atRAN. In contrast, both APOs@^{atRAN}NP$_{miR\text{-}124}$ and APOs@^{atRAN}BP$_{miR\text{-}124}$ without H_2O_2 pretreatment provided limited inhibition of glial differentiation due to difficulty in miR-124 release. Of note, APOs@^{atRAN}BP$_{miR\text{-}124}$ treatment resulted in the highest neural differentiation efficiency up to 72.6% with negligible glial differentiation (only 4.8%). Similar expression variations of MAP2 and GFAP were observed in western blot analysis, which further confirmed the capability of APOs@^{atRAN}BP$_{miR\text{-}124}$ to direct stem-cell neural differentiation (Fig. 3g, h). Thereafter, a cytoplasmic fluorescent dye (calcein-AM) was introduced for visualization of morphological changes of differentiated cells. As shown in Fig. 3i, j, cells in control group were short and fusiform (22.2 μm of protrusion length), while cellular protrusion length in different complexes-treated groups gradually increased. When treated with APOs@^{atRAN}BP$_{miR\text{-}124}$ (with H_2O_2 pretreatment), eMSCs demonstrated more neuronal somas with a remarkable increase to 119.4 μm in protrusion length than other H_2O_2-pretreated groups, including APOs@^{atRAN}NP$_{miR\text{-}124}$, APOs@BP$_{miR\text{-}124}$ and APOs@^{atRAN}BP$_{miR\text{-}NC}$, as well as APOs@^{atRAN}BP$_{miR\text{-}124}$ without H_2O_2 pretreatment. These findings suggest that the sequential release of atRAN and miR-124 from APOs@^{atRAN}BP$_{miR\text{-}124}$ orchestrates an efficient neural differentiation of MSCs within an AD pathological microenvironment.

In addition to neuron-specific markers and neuron-like morphology, the key to neural differentiation lies in performing neuronal functions, especially transmitting signals of calcium ion (Ca^{2+}) and electrophysiological activity. Consequently, we conducted intracellular calcium imaging using Fluo-4 AM, a fluorescent probe that emits visible fluorescence upon binding Ca^{2+}. Calcium responses to depolarization were evaluated by monitoring fluorescence changes over time following stimulation with 50 mM KCl (a depolarization inducer). In contrast to PBS-MSCs with negligible changes of intracellular Ca^{2+} levels, APOs@^{atRAN}BP$_{miR\text{-}124}$-eMSCs displayed recurrent fluorescence changes, indicating their response to depolarization and the presence of voltage-dependent calcium channels (Fig. 3k). Consequently, electrophysiological analysis of APOs@^{atRAN}BP$_{miR\text{-}124}$-eMSCs was further performed using a patch-clamp. During depolarization voltage steps, PBS-MSCs exhibited weak voltage dependency, producing only small, noise-like outward current signals due to the lack of typical voltage-gated sodium, potassium, and calcium channels. In contrast, applying a series of voltage steps to APOs@^{atRAN}BP$_{miR\text{-}124}$-eMSC-derived cells evoked a substantial and consistent increase in voltage-dependent current amplitude. The response, characterized by initial inward currents followed by outward currents, reflected sodium influx and potassium efflux, respectively, indicating the presence of voltage-dependent ion channels and fundamental electrophysiological functionality (Fig. 3l). Thus, the results indicate that APOs@^{atRAN}BP$_{miR\text{-}124}$ can direct MSC differentiation into neuron-like cells with physiological functions.

Mechanisms of enhanced neural differentiation of eMSCs

To systematically elucidate the underlying molecular mechanism of APOs@^{atRAN}BP$_{miR\text{-}124}$ in managing neural differentiation of MSCs, we performed RNA sequencing on APOs@^{atRAN}BP$_{miR\text{-}124}$-eMSCs with untreated MSCs set as control. A comparison of gene expression between the two groups revealed 5275 differentially expressed genes (DEGs), of which 3123 genes were upregulated and 2152 genes downregulated (Supplementary Fig. 22). As shown in Fig. 4a, gene ontology (GO) enrichment analysis indicated that the upregulated genes were associated with retinoic acid binding, response to retinoic acid, neuron differentiation, neuron projection, and neuron maturation, etc. In contrast, the downregulated genes were mainly enriched in cell proliferation and negative regulation of neuron differentiation. The results indicated the transition of APOs@^{atRAN}BP$_{miR\text{-}124}$-eMSCs from cell proliferation to differentiation induced by atRAN, and activation of neuron-specific transcriptional programs induced by miR-124, respectively. The Kyoto Encyclopedia of Genes and Genomes (KEGG) enrichment analysis further revealed DEG enrichment in pathways related to neural differentiation (e.g., cGMP-PKG, MAPK, and PI3K-Akt signaling pathways) and neuron development (e.g., axon guidance, cholinergic synapse, glutamatergic synapse, synaptic vesicle cycle, and neuroactive ligand-receptor interaction) (Fig. 4b). Therefore, DEGs ($n = 184$) involved in these process were selected and clustered in a heatmap, with their gene interactions determined using STRING analysis (Fig. 4c, d). The majority of these DEGs exhibited coordination with each other and formed an interaction network. As shown in Fig. 4e, APOs@^{atRAN}BP$_{miR\text{-}124}$ treatment down-regulated genes involved in inhibition of neuron differentiation and development (e.g., *DPYSL3*, *GFI1*, *HES1*, *ZHX2*, *FAT3*, and *EDNRB*), while up-regulating the genes related to positive regulation of neurogenesis (e.g., *MAPT* and *APOE*), neuronal cell body (e.g., *MAP2* and *NCAM1*), and neuron maturation (e.g., *LGI4* and *CDKN1C*), indicating the directional eMSC differentiation into neurons. These findings reveal that APOs@^{atRAN}BP$_{miR\text{-}124}$ treatment activates retinoic acid signaling pathway and cGMP-PKG, MAPK, and PI3K-Akt signaling pathways for neurogenesis via up-regulating neuronal genes (e.g., *MAPT*, *MAP2*, and *CDKN1C*) and suppressing negative regulators (e.g., *ZHX2*, *HES1*, and *EDNRB*), directing MSCs toward a mature neuronal fate.

Survival and differentiation of eMSCs in vivo

The survival and differentiation fate of transplanted eMSCs as exogenous grafts in the brain need to be examined in terms of safety and efficacy in vivo[25]. Hence, 2.5 μL of different eMSCs suspension were transplanted into each hippocampus of APPswe/PS1dE9 (APP/PS1)

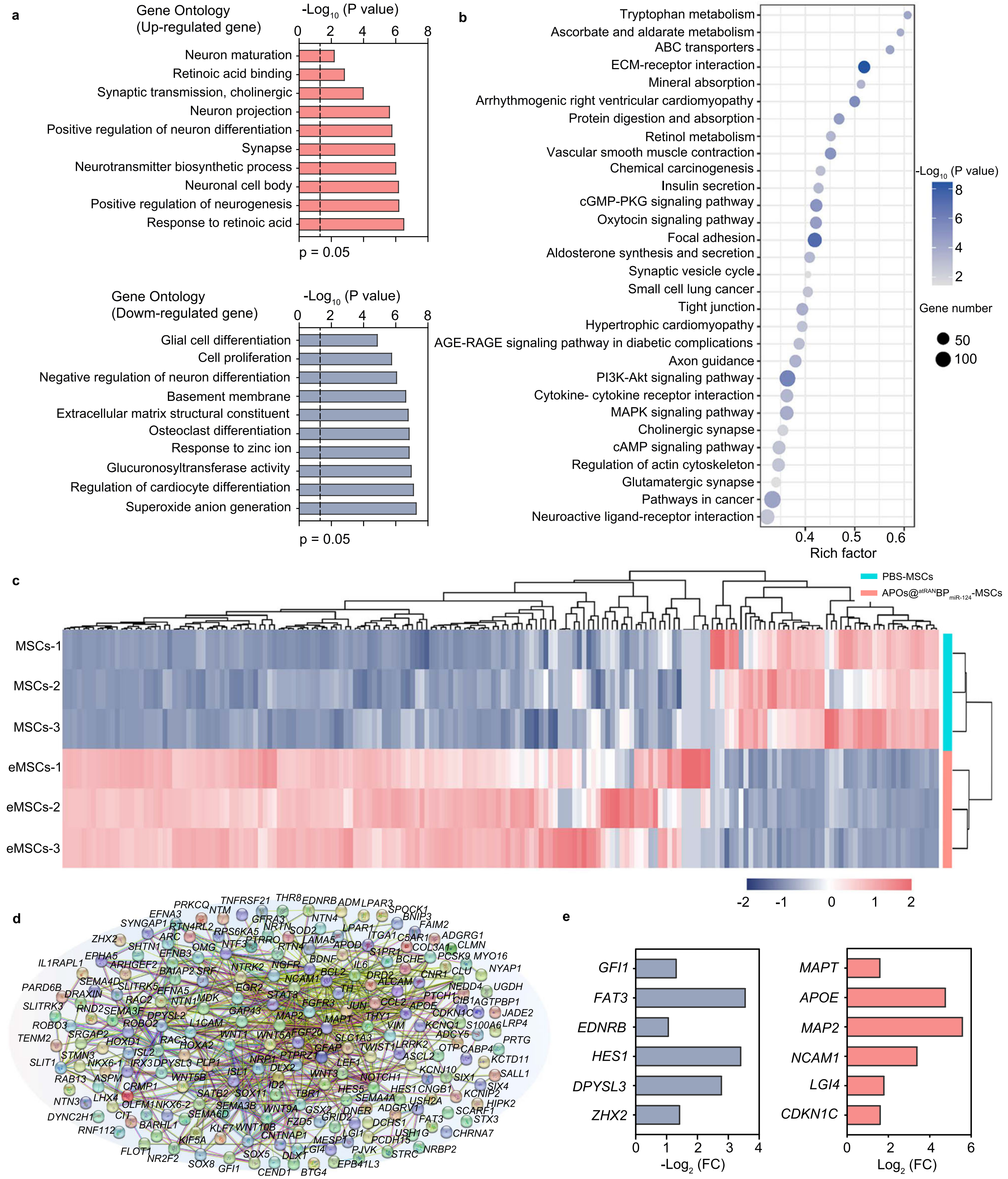

Fig. 4 | Mechanisms underlying the augmented neural differentiation of APOs@$^{\mathrm{atRAN}}$BP$_{\mathrm{miR\text{-}124}}$-eMSCs. a GO analysis of functional annotations of DEGs, including up-regulated and down-regulated genes. DEGs were identified with a fold change (FC) of ≥ 2 and a false discovery rate (FDR) of ≤ 0.05. **b** KEGG analysis of enriched pathways identified in MSCs and APOs@$^{\mathrm{atRAN}}$BP$_{\mathrm{miR\text{-}124}}$-eMSCs, respectively. **c** Heatmap showing gene expression profiles of 184 DEGs involved in neurogenesis via hierarchical clustering analysis ($n = 3$ independent samples). **d** STRING analysis for 184 DEGs involved in neurogenesis revealing gene-gene interaction networks. **e** Representative genes involved in negative (left) and positive (right) neurogenesis, respectively. Fisher's exact test and Benjamini-Hochberg correction for multiple comparisons were used for statistical analysis of (**a**, **b**). Source data are provided as a Source Data file.

transgenic AD model mice via intracerebral injection. Brain tissues were harvested 30 days post-transplantation for histological analysis (Supplementary Fig. 23). Haematoxylin-eosin (HE) staining revealed no malignant findings such as abnormal hyperplasia or necrosis around the hippocampal region (Fig. 5a), indicating desirable safety profiles for eMSC transplantation. To investigate whether the transplanted eMSCs elicited an immune response that would accelerate removal of exogenous cells, immunostaining analysis was performed to detect

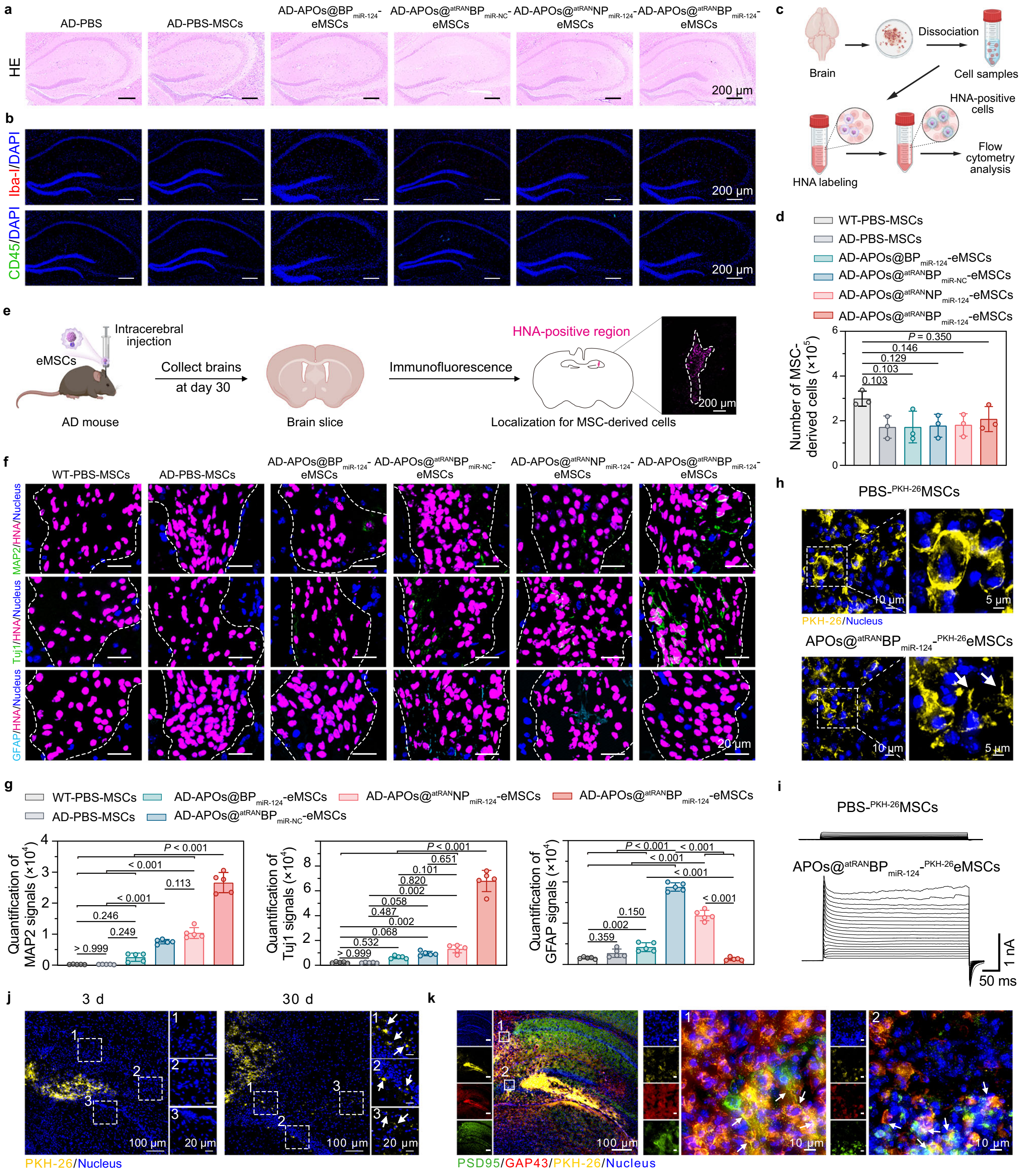

infiltration of immune cells in brain, including microglia and leukocytes, with proinflammatory lipopolysaccharide (LPS) treatment serving as a positive control group. Contrary to the brain of wild-type (WT) mice, elevated Iba-1 and CD45 signals were observed in the hippocampus of all brains of APP/PS1 mice, irrespective of eMSC transplantation, indicating increased immune cell activity in AD pathology (Fig. 5b and Supplementary Fig. 24). Unlike the robust immune response elicited by LPS, eMSC transplantation did not further elevate or accumulate immune cells, suggesting that eMSC transplantation would not induce immune-mediated clearance in brains of APP/PS1 mice. To quantitatively assess the survival of MSC-derived cells in the brain, brain tissues were collected to extract all cells at 30 days after transplantation, followed by cell labeling using antibodies against human nuclear antigen (HNA) to detect the total number of HNA positive (HNA +) cells by using flow cytometry analysis (Fig. 5c). As shown in Fig. 5d and Supplementary Fig. 25, the percentage of eMSCs in brains of APP/PS1 mice slightly decreased compared to that in the normal brain of wide-type (WT) mice, indicating the adverse impact of pathological environment on transplanted cell survival. Nonetheless, the percentage of APOs@^{atRAN}BP$_{miR-124}$-eMSCs (HNA +) out of the total brain cells was 0.2% (with an average number of approximately 2.1 × 10^5), representing about 8.4% of the initially transplanted cells, with no

Fig. 5 | APOs@^{atRAN}BP$_{miR-124}$-eMSCs survived and differentiated into neurons in vivo. a Representative images of HE staining in the hippocampus after transplantation of MSCs and different eMSCs. The sham operation group without cell injection was used as the control group. **b** Immunofluorescent detection for Iba-1 (red) and CD45 (green) to label microglia and leukocytes in brain, respectively. The PBS-treated AD group without cell injection was used as control. **c** Illustration of detection of MSC-derived cells from brain tissue collection[30]. **d** Quantitative analysis of MSCs and different eMSCs in brain. **e** Illustration of detection of MSC-derived cells in the brain slices. MSC-derived cells were localized through HNA-positive regions. The immunofluorescence image on the right is derived from the black dashed box region[31]. **f** Immunostaining of brain slices for neural-specific markers Tuj1 (green) and MAP2 (green) and glial-specific marker GFAP (bright blue) after implantation of MSCs and different eMSCs (HNA + , pink) for 30 days, respectively. White dotted lines indicate the graft. **g** Quantification of fluorescence signal of MAP2, Tuj1, and GFAP. **h** Morphology of transplanted PBS-$^{PKH-26}$MSCs (yellow) and APOs@^{atRAN}BP$_{miR-124}$-$^{PKH-26}$eMSCs (yellow) in brains of APP/PS1 mice 30 days post-transplantation, respectively. The white dashed box indicates the magnified region. **i** Representative voltage-dependent membrane currents of PBS-$^{PKH-26}$MSCs and APOs@^{atRAN}BP$_{miR-124}$-$^{PKH-26}$eMSCs in the brain slices. **j** Representative fluorescence images showing the position of transplanted APOs@^{atRAN}BP$_{miR-124}$-$^{PKH-26}$eMSCs (yellow) in the brains of APP/PS1 mice at 3 days and 30 days post-transplantation, respectively. The white dashed box indicates the magnified region and the white arrows indicate PKH-26 positive cells. **k** Immunostaining of brain slices for presynaptic marker GAP43 (red) and the postsynaptic marker PSD95 (green) after transplantation of APOs@^{atRAN}BP$_{miR-124}$-$^{PKH-26}$eMSCs (yellow) for 30 days, respectively. The solid white wire boxes indicate the magnified regions and the white arrow refers to the synapse formation between transplanted eMSCs with host cells. Data were presented as mean ± SD ($n = 3$ mice in **d**; $n = 5$ mice in **g**). One-way ANOVA with Tukey post-hoc test was used for statistical analysis of **d**, **g**. Three independent experiments were performed with similar results and representative results are shown (**a**, **b**, **h**, **j**, **k**). Source data are provided as a Source Data file.

significant difference from other groups in brains of APP/PS1 mice. These findings imply the safety and long-term survival of APOs@^{atRAN}BP$_{miR-124}$-eMSCs in the brain, ensuring sufficient period for differentiation and following efficacy.

Immunostaining for neuron-specific markers (Tuj1 and MAP2) and astrocytes-specific marker (GFAP) was further performed to analyze eMSC differentiation in vivo. The HNA-positive regions in the hippocampus were selected to locate MSC-derived cells and observe them (Fig. 5e). As demonstrated in Fig. 5f, g, PBS-MSCs and APOs@BP$_{miR-124}$-eMSCs rarely differentiated into neurons (Tuj1/MAP2-positive cells) or astrocytes (GFAP-positive cells) in either normal brains of WT mice or brains of APP/PS1 mice, due to the lack of atRAN-mediated differentiation initiation signals. GFAP-positive fluorescent signals were detected in APOs@^{atRAN}BP$_{miR-NC}$-eMSCs and APOs@^{atRAN}NP$_{miR-124}$-eMSCs groups, indicating their unavoidable glial differentiation fate. In contrast, most of HNA-labeled cells in APOs@^{atRAN}NP$_{miR-124}$-eMSCs group were estimated to be Tuj1 and MAP2 positive without GFAP signal, confirming high potential of APOs@^{atRAN}BP$_{miR-124}$ to control directional neuron differentiation of MSCs. Thereafter, the morphology of APOs@^{atRAN}BP$_{miR-124}$-eMSCs in the brain was also assessed by pre-labeling with PKH-26, a membrane dye for live cells with a long in vivo labeling half-life, using PBS-MSCs as a control group. As shown in Fig. 5h, PKH-26-labeled MSCs (PBS-$^{PKH-26}$MSCs) appeared smooth and rounded at 30 days post-transplantation, while APOs@^{atRAN}BP$_{miR-124}$-$^{PKH-26}$eMSC-derived cells displayed irregular shapes with protrusions or branching structures, reflecting the morphological transformation associated with neural differentiation in vivo. Moreover, the results of electrophysiological analysis further confirmed the in vivo electrophysiological activity of cells differentiated from APOs@^{atRAN}BP$_{miR-124}$-$^{PKH-26}$eMSCs (Fig. 5i). The observed changes in current signals, initially decreasing and then increasing, indicated the presence of rapidly activated inward sodium and outward potassium currents. These findings indicate neural differentiation and function maturation of APOs@^{atRAN}BP$_{miR-124}$-eMSCs in vivo.

Moreover, we noticed that the transplanted APOs@^{atRAN}BP$_{miR-124}$-eMSCs were initially localized at the injection site 3 days post-transplantation, but were dispersed and detected in other hippocampal regions 30 days later, demonstrating their migratory capability and supporting neuron replacement and repair across multiple lesion sites within the brains of APP/PS1 mice (Fig. 5j). Consequently, their synaptic formation and integration with host cells were further evaluated using immunostaining for the presynaptic marker GAP43 (in red) and the postsynaptic marker PSD95 (in green), with transplanted APOs@^{atRAN}BP$_{miR-124}$ labeled by PKH-26 (in yellow). As demonstrated in Fig. 5k, obvious colocalization of GAP43, PSD95, and PKH-26 was observed, demonstrating that APOs@^{atRAN}BP$_{miR-124}$-eMSC-derived cells could form synapses in the hippocampus. Additionally, PKH-26-positive transplanted cells also co-localized with adjacent host cells (PKH-26-negative but GAP43-positive or PSD95-positive) in the DG and CA1 regions, indicating their integration and synapse formation with host cells in the hippocampus of brains of APP/PS1 mice. Notably, while PKH-26 used in this study is not perfect to completely avoid dye transferring to host cells in some cases (e.g., MSC apoptosis, fusion, trogocytosis, or vesicles/exosomes transfer), the overall impact of such intercellular transfer was minimal. Developing a more stable labeling method for MSC tracing to eliminate host signal interference is encouraged.

Collectively, APOs@^{atRAN}BP$_{miR-124}$-eMSCs share desirable safety, long-term survival, and high potential of neural differentiation, migration, and synapse formation with host cells in vivo, further supporting the application to reconstruct damaged neural circuit for AD treatment.

eMSCs ameliorated cognitive decline of AD model mice via neuron regeneration

Considering capability of eMSCs in long-term survival in brain and efficient neural differentiation, we determined to investigate the therapeutic efficacy of APOs@^{atRAN}BP$_{miR-124}$-eMSCs on APP/PS1 mice after single dose. One month after stereotactic transplantation of eMSCs into hippocampus, the memory, and cognitive functions of AD model mice were evaluated using Morris water maze (MWM) assays and nesting behavior, respectively (Fig. 6a). In MWM assays, in contrast to other groups with a minor degree of learning improvement, APOs@^{atRAN}BP$_{miR-124}$-eMSC administration resulted in the most significant amelioration in learning and cognitive ability of AD model mice, as evidence of high platform searching performance with shorter latency (23.0 s), more crossing times (5.4 T) and longer stay (40.8%) at the target quadrant (Fig. 6b, c). Besides, the hippocampal function of AD model mice was assessed using the nesting behavior assay. As shown in Fig. 6d, e, while PBS-treated AD model mice failed to build a complete and mass nest, APOs@^{atRAN}BP$_{miR-124}$-eMSCs treated AD model mice displayed excellent nesting skills with a close score to the WT mice, suggesting that APOs@^{atRAN}BP$_{miR-124}$-eMSCs could remarkably improve hippocampal functions in AD model mice.

Thereafter, we sought to verify that the observed memory improvement induced by APOs@^{atRAN}BP$_{miR-124}$-eMSCs was associated with their neural regeneration effects. The brain tissues were collected and analyzed using immunostaining for human doublecortin (hDCX) to assess human neurogenesis in AD model mice. Non-human-specific synaptophysin (SYP) was chosen to evaluate synaptic activity, due to the cross-reactivity of commercially available anti-human SYP antibodies with host SYP. Compared to AD-MSCs group, a significant increase in hDCX-labeled newborn neurons in the dentate gyrus and enhanced overall synaptic activity marked by SYP in the hippocampus were observed following APOs@^{atRAN}BP$_{miR-124}$-eMSC treatment (Fig. 6f, g). The transplanted MSCs were expected to not only

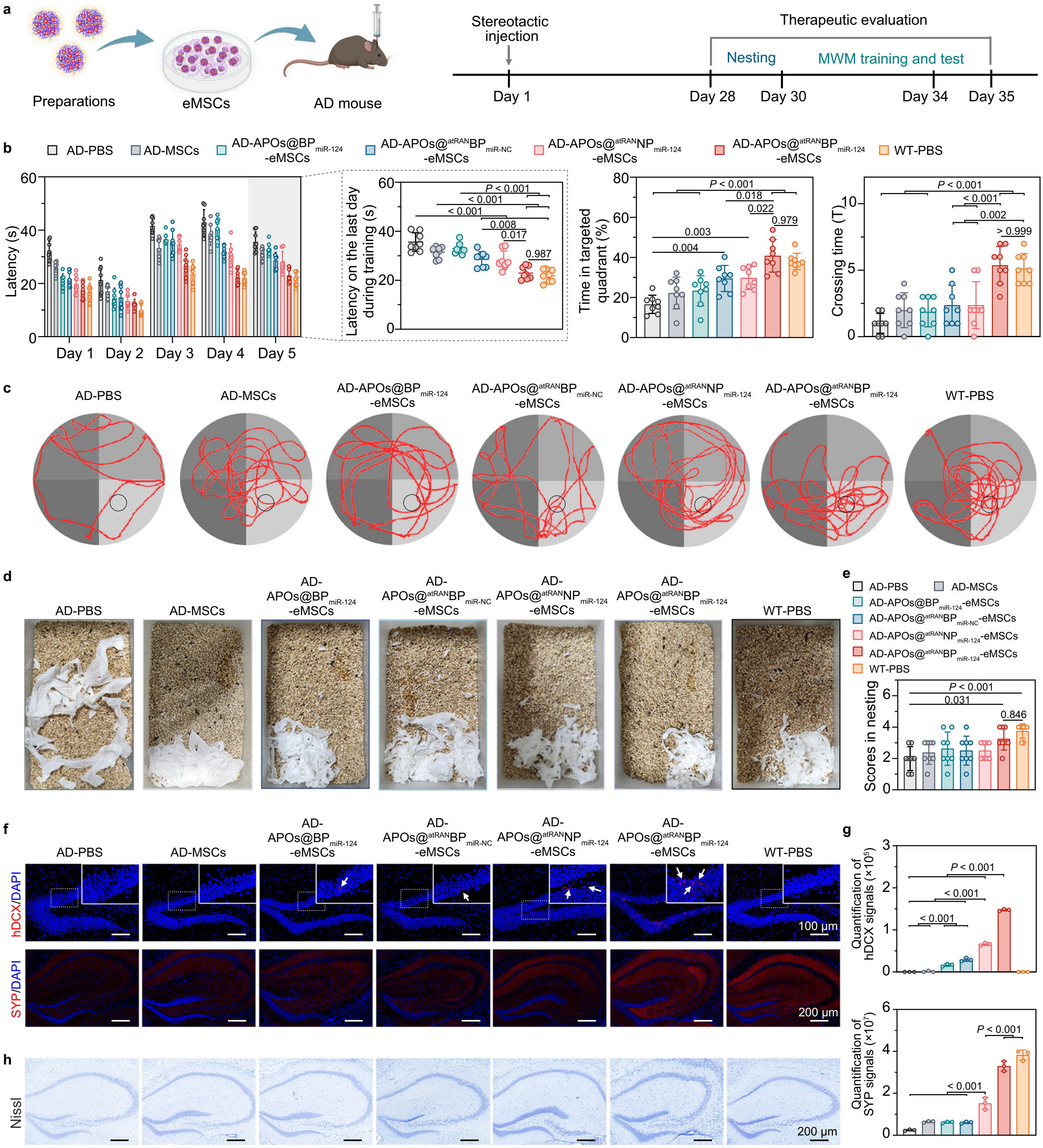

Fig. 6 | APOs@^{atRAN}BP$_{miR-124}$-eMSCs improved cognitive and memory impairments of AD model mice. a Time scheme of different eMSC treatment and therapeutic assessment[29]. **b** The latency, percent time spent in the targeted quadrant, and crossing time of mice in MWM test. **c** The representative swimming path tracings of mice. **d** Representative images of nest behaviors. **e** Scores of nest behaviors for each group. **f** Immunofluorescent detection for hDCX (red) and overall SYP (red) to label MSC-derived immature neurons and the entirety of synaptic activity, respectively. The white dashed box indicates the magnified region and white arrows indicate hDCX-positive cells. **g** Quantification of the fluorescence signal of hDCX and overall SYP. **h** Representative images of Nissl staining. Data were presented as mean ± SD ($n = 8$ mice in **b**, **e**; $n = 3$ mice in **g**). One-way ANOVA with Tukey post-hoc test was used for statistical analysis of **b**, **e**, **g**. Representative is displayed from three independent experiments. Source data are provided as a Source Data file.

differentiate into neurons but, critically, establish synaptic connections with host cells, directly enhancing overall synaptic activity between donor and host neurons. Although direct measurement of human SYP levels is currently unattainable, the result demonstrated a positive correlation between overall synaptic activity and the neurogenic capacity of transplanted eMSCs, indirectly supporting their intrinsic connection and allowing for an intuitive evaluation of neural activity recovery post-treatment by directly comparing with normal wild-type mice. Future development of better species-specific methods to directly evaluate human synaptic activity in mouse brains would represent a significant advancement. Besides, Nissl staining also demonstrated that APOs@^{atRAN}BP$_{miR-124}$-eMSC treatment increased the number of neurons with intact nuclei in hippocampus compared to other MSC groups (Fig. 6h). The encouraging results indicate that APOs@^{atRAN}BP$_{miR\text{-}124}$-eMSCs can improve neural regeneration and synaptic connections in brains of APP/PS1 mice.

Discussion

The critical challenges of MSC engineering in regenerative therapies are the limited transfection efficiency and poor safety profiles. Particularly, serum-protein adsorption of transfectant agents seriously impedes cytomembrane interactions during MSC culture, leading to sacrificed transfection efficiency. Hence, most MSC transfection are operated in absence of serum, but it will cause cell damage, leading to poor therapeutic efficacy. To resolve this contradiction, our study provides a serum-defense polymeric complex to achieve serum-tolerant MSC transfection with desirable transfection efficiency and safety profiles. The protocol is simple to manipulate in that ROS-responsive boronated PEI effectively compresses miRNA via electrostatic interaction and coordinates with APOs to form a polymeric complex with a core-shell structure via simple mixing. The polymeric complex shared superior efficiency in transfecting MSCs with biostability and biocompatibility in the presence of serum compared to polycationic transfectants with higher molecular weight (Fig. 2a–e). The promising transfection efficiency was ascribed to serum-protein resistance induced by the steric hindrance of APOs and complexes-cytomembrane interaction triggered by conformational transition of α-helical regions in APOs (Fig. 2f, h–j). Moreover, the immediate lysosomal escape and ROS-responsive degradation characteristics of APOs@BP promoted cytosolic release of miRNA, leading to highly efficient transfection (Fig. 2l, m). Therefore, APOs@BP could be deemed to be a promising reagent for effectively serum-tolerant MSC transfection via integrating miRNA compression and on-demand release performance. Moreover, APOs@BP provides enough reservoirs for drug shielding, making it possible to manufacture MSC engineering via multi-element cooperation. Recent studies demonstrate that MSCs can differentiate into neural lineage cells, as indicated by the expression of neural lineage-specific markers and the development of neuronal-like morphological and functional traits under certain conditions. However, their intrinsic efficiency for neural differentiation is relatively low and less controllable compared to neural stem cells, making their neural differentiation challenging. To improve and regulate MSC neural differentiation, APOs@BP was further employed to integrate all-trans retinoic acid derivative (atRAN) together with miR-124 to activate differentiation potential and neuron-specific programming, respectively.

After simple incubation, atRAN and miR-124 were assembled into APOs@BP via boron-nitrogen coordination and electrostatic compression to form APOs@^{atRAN}BP$_{miR\text{-}124}$ (Fig. 3a, b). As confirmed, APOs@^{atRAN}BP$_{miR\text{-}124}$ released atRAN initially upon escape from acidic lysosomes after cellular internalization (Fig. 3c); when exposed to infiltrated ROS following MSC transplantation into AD lesion sites, polymeric complexes degraded and discharged miR-124 (Fig. 3d). In accordance with neural differentiation programs, such a sequential regulation of MSC engineering significantly boosted directional neural differentiation of MSCs via activation of retinoic acid signaling and cGMP-PKG, MAPK, and PI3K-Akt signaling pathways (Figs. 3e–l, 4a, b and 5f–i). Moreover, both in vitro and in vivo studies demonstrated that APOs@^{atRAN}BP$_{miR\text{-}124}$-eMSC-derived cells showed neuron-specific marker, elongated cell bodies, and electrophysiological features (Figs. 3e–l and 5f–i). In addition, APOs@^{atRAN}BP$_{miR\text{-}124}$-eMSC-derived cells demonstrated the ability to migrate and form synapses with host cells, enhancing neural regeneration and increasing synaptic connections in the brains of APP/PS1 mice (Figs. 5j, k, and 6f–h). This led to a recovery of pathologic behaviors in AD model mice (Fig. 6b–e).

Collectively, APOs@BP provides an easy-to-apply and highly efficient approach for MSC transfection with desirable safety profiles. In addition to MSC differentiation, APOs@BP can be utilized to modify MSCs for other biomedical applications, such as living cell carriers for targeted drug delivery, or in-situ production of proteins and engineered exosomes. Beyond MSC engineering, APOs@BP might be further extended to customization of other types of "living cell" therapeutics, for example, immune cell engineering and manufacturing against cancer.

Methods

Cells

MSCs·were isolated from human umbilical cords and·cultured in·commercially available serum-free human-MSC medium (TBD, SC2013-G) containing 10% nutritional factor additive provided with the kit. The human umbilical cords were obtained from healthy women with full-term pregnancy. The donors provided signed informed consent, and the procurement process was approved by the Ethics Committee of the Affiliated Hospital of Jiangnan University. The cells were cultured in Dulbecco's Modified Eagle Medium·(DMEM, Pricella Life Science&Technology Co., Ltd, PM150210) during transfection. The engineered MSCs were cultured in Neurobasal medium containing·2% B-27 supplement (Yeasen, 60711ES), 0.5 mM glutamine (Gibco, 25030081), 1% FBS (Gibco, 10091148), and 1% penicillin-streptomycinand (absin, abs9244) in a humidified atmosphere at 37 °C with 5% CO_2. The culture medium was changed every two days.

Animals

Male 10-month-old·APPswe/PS1dE9 mice and C57BL/6 wild-type mice were purchased from Aniphe BiolaboratoryInc and Phenotek Biotechnology (Shanghai, China). The animals were maintained on a standard diet with water ad libitum at 23 °C and 45-55% relative humidity with a 12-12 h light-dark cycle and complied with the requirements·of the Animal Experimentation Ethics Committee of China Pharmaceutical University (approval number 2023-06-004).

Antibodies

The used antibodies were as follows: PE-anti-human CD34 antibody (Elabscience, 581, E-AB-F1143D), PE-anti-human CD45 antibody (Biolegend, HI30, 304007), FITC-anti-human CD44 antibody (Elabscience, P2A1, E-AB-F1038C), FITC-anti-human CD90-antibody (Biolegend, 5E10, 328107), FITC-anti-human CD105 antibody (Biolegend, 43A3, 323203), anti-Wnt2b antibody (Zenbio, R26109), anti-GFAP antibody (Proteintech, 60190-1-Ig), anti-Iba1 antibody (Servicebio, GB113502), anti-Tuj1 antibody (Abcam, ab18207), anti-CD45 antibody (Bioss, bs-4819R), anti-MAP2 antibody (Cell SignalingTechnology, 4542), anti-human nuclear antigen antibody (Abcam, ab191181), anti-NeuroD1 antibody (Abcam, ab213725), anti-PSD95 antibody (Abcam, ab18258), anti-GAP43 antibody (Abcam, ab75810), anti-human DCX antibody (Novus Biologicals, NBP2-69992), anti-synaptophysin antibody (Servicebio, GB14150-50), HRP-labeled sheep anti-rabbit IgG (Servicebio, GB23303), HRP-labeled sheep anti-mouse IgG (Servicebio, GB23301), HRP-labeled rabbit anti-goat IgG (Servicebio, GB23204), FITC-labeled sheep anti-rabbit IgG (Servicebio, GB25303), Alexa Fluor 594-labeled sheep anti-mouse IgG (abcam, ab150116), and goat anti-mouse IgG/SAlexa Fluor 488 (Solarbio, K0031G-AF488).

Synthesis and characterization of ROS-responsive boronated PEI

PEI (1.08 g) was dissolved in deionized water (2 mL) and dropped into formic acid (8 mL), followed by adding formaldehyde (8 mL). The mixture was reacted at 95 °C for 8 h. The solvent was removed by rotary evaporation and the residue was dissolved in 8 mL methanol. The solvent was removed by rotary evaporator after the reaction and the primary product was redissolved in methanol (8 mL). After filtration to remove insoluble impurities, the product was redissolved in methanol to obtain a tertiary aminated PEI (tert-PEI) solution. tert-PEI

(200 μL) was reacted with 4-(bromomethyl) phenylboronicacid (65 mg) in dimethylformamide (DMF) for 24 h in the dark. The mixture was stirred in the dark for 24 h, followed by dialysis (MWCO = 3500 Da) and lyophilization to obtain BP polymers. The chemical structure of BP and the substitution degree of PBA were characterized by ^{1}H NMR spectra and gel permeation chromatography (GPC).

miRNA transfection

MSCs were seeded and cultured in a 24-well plate (1×10^4 cells per well) for 24 h prior to transfection. Different polymers, including ^{10K}PEI, ^{25K}PEI, BP, and APOs@BP, compressed FAM-labeled miRNA (FAM-miRNA, RIBOBIO, miR01104-1-1) at their optimized N/P ratios and dissolved in DMEM containing 0 or 10% FBS to maintain a final miRNA concentration of 120 nM, which were then incubated with MSCs for 6 h. The transfected MSCs were washed three times with PBS and observed using an inverted fluorescence microscope (Eclipse Ts2-FL, Nikon Precision Inc., CA, USA). The uptake efficiency and positive cell rate were analyzed using a flow cytometer.

Membrane binding with giant unilamellar vesicles (GUVs)

GUVs labeled with DiI (Beijing Solarbio Science & Technology Co., Ltd., D8700) were prepared as the following methods. Briefly, bisacrylamide solution was coated and polymerized on glass slides for 2 h, followed by drying in an oven for 10 min. A mixture of lipid solutions (phosphotidylcholine in chloroform/methanol (volume ratio of 3:1) at 5 mg mL^{-1}, 1% DiI, 30 uL) was spread onto the gel, followed by solvent evaporation in a vacuum for 15 min. 1 mL 0.6 ml of 100 mM sucrose was added and incubated overnight at 37 °C. The collected GUV solution was diluted 10 times through 150 mM glucose solution. The GUVs were incubated with FAM-labeled APOs@BP$_{miRNA}$ and BSA@BP$_{miRNA}$ for 6 h, respectively. The membrane binding of nanoparticles was visualized using confocal laser scanning microscopy (CLSM, LSM700, Carl Zeiss AG, Oberkochen, Germany).

Preparation and characterization of APOs@^{atRAN}BP$_{miR\text{-}124}$

The BP polymer was mixed with miR-124 (5′-UAAGGCACGCGGUGAAUGCCAA-3′) (RIBOBIO, China) by vortex at a N/P ratio of 1. Subsequently, 120 μL of APOs solution (1 mg mL^{-1}) was added and stirred for 30 min. 100 μL atRAN·HCl solution (0.4 mg mL^{-1}) was added drop by drop, followed by adding 15 μL $NaHCO_3$ solution (10 mg mL^{-1}) to facilitate coordination between BP and atRAN. After incubation for 12 h at 37 °C, APOs@^{atRAN}BP$_{miR\text{-}124}$ was obtained after ultrafiltration to remove unbounded drugs. The particle size and polydispersity index (PDI) of APOs@^{atRAN}BP$_{miR\text{-}124}$ were measured using DLS and the morphology was observed by TEM. The formation of boron and nitrogen coordination between atRAN and BP was assessed using X-ray photoelectron spectroscopy (XPS; 5000 VP II, ULVAC-PHI, Inc., Japan). To analyze the entrapment efficiency (EE%) and the drug loading (DL%), the filtrate containing unbounded atRAN was collected, of which the absorbance was measured by UV-spectrophotometer at 353 nm.

The EE% and DL% were calculated using the following formula: EE% = (the total amount of atRAN before ultrafiltration-the amount of atRAN in the filtrate) / (the total amount of atRAN before centrifugation) × 100%; DL (%) = (the total amount of atRAN before ultrafiltration - the amount of atRAN in the filtrate) / (the total quality of APOs@^{atRAN}BP$_{miR\text{-}124}$) × 100%.

Cell differentiation assay

MSCs were seeded and cultured in a 24-well plate (1×10^4 cells per well) for 24 h prior to transfection. The MSCs were cultured in commercially available neurobasal medium supplemented with 2% B-27, 0.5 mM glutamine, and 1% penicillin-streptomycin for 30 days, with 1% FBS added to support basic cell activity without promoting proliferation during differentiation. The culture was maintained in a humidified environment at 37 °C and 5% CO_2, with medium changes every two days. Neural differentiation capacity of MSCs was evaluated by immunofluorescence staining. The differentiated cells were fixed with 4% paraformaldehyde for 15 min. The cells were then permeabilized with 0.2% Triton X-100 for 20 min at room temperature, followed by being rinsed three times in PBS and then blocked with 3% (v/v) bovine serum albumin solution for 30 min at room temperature. For MAP2 analysis, the cells were incubated with anti-MAP2 antibody at 4 °C overnight and then washed three times with PBS, followed by incubation with FITC-labeled sheep anti-rabbit IgG at 37 °C for 50 min. For GFAP analysis, the cells were incubated with anti-GFAP antibody at 4 °C overnight, followed by incubating with Alexa Fluor 594-labeled sheep anti-mouse IgG at 37 °C for 50 min. The cells were washed with PBS and then stained with DAPI for 8 min in the dark. The cells were observed using CLSM.

Ca^{2+} imaging

The cellular calcium dynamics were monitored using the Fluo-4 Calcium Imaging Kit (Beyotime Biotechnology, S1061S) to assess the neural activity of the differentiated cells. After being washed three times with HBSS, the cells were added with Fluo-4 AM staining solution (5 μM) and incubated for 30 min at 37 °C in the dark. After incubation, the cells were washed once in HBSS. After a physiological buffer containing 50 mM KCl was added, the dynamics of the fluorescence intensity in the differentiated cells were monitored using CLSM.

Membrane current detection

An Axon 700B amplifier (Axon) was used to detect the membrane current. The signal was filtered at 2 kHz and digitized to 10 kHz for current recording. The recording electrodes were filled with a solution (140 mM K-gluconate, 5 mM NaCl, 2 mM Mg-ATP, 0.5 mM LiGTP, 0.1 mM $CaCl_2$, 1 mM $MgCl_2$, 1 mM EGTA, and 10 mM HEPES at pH 7.25). The cells were exposed to an external solution (140 mM NaCl, 3.5 mM KCl, 1.25 mM NaH_2PO_4, 2 mM $CaCl_2$, 1 mM $MgCl_2$, 10 mM glucose, and 10 mM HEPES at pH 7.4) to record the currents. The cells were clamped at -70 mV and depolarized from -120 mV to +80 mV in 500 ms using the voltage clamp mode of the whole-cell patch-clamp technique. For the current detection of transplanted cells in the brain, the transplanted cells were pre-labeled with PKH-26 using the PKH26 Red Fluorescent Cell Linker Kit (APExBIO, Houston, USA, K2410). The PKH-26 integrated into cell membranes via its long aliphatic chain and persisted (half-life > 100 days). Thirty days post-transplantation, brain tissue was harvested, and acute coronal slices with a thickness of 300 μm were prepared using a vibratome. The slices were immersed in artificial cerebrospinal fluid (124 mM NaCl, 3 mM KCl, 1.25 mM $NaH_2PO_4 \cdot 2H_2O$, 26 mM $NaHCO_3$, 10 mM Dextrose, 1 mM $MgCl \cdot 6H_2O$, and 2 mM $CaCl_2$). PKH-26-positive cells in brain slices were visualized using fluorescence imaging. The exposure time was optimized through the assessment of corresponding fluorescence signal intensity and background noise levels, aiming to reduce background interference while avoiding excessive exposure to minimize potential cell damage. An exposure time of 100 ms was selected to identify PKH-26-positive cells in brain slices. During the experiment, PKH-26-positive cells are identified within 5-10 seconds in fluorescence imaging mode to reduce potential cell damage and prevent quenching, followed by switching to the non-fluorescent testing mode and testing electrophysiological activity using the same procedure. Voltage-clamp membrane currents were recorded from 16 PKH-26-positive transplanted cells (from brain slices of 4 mice) per group. The recorded cells were randomly sampled and strictly selected based on three key criteria: high and uniform PKH-26 fluorescence on the membrane to avoid misjudgment due to intercellular transfer; intact and plump morphology, excluding shriveled or damaged cells; and even distribution within the hippocampal transplant site to prevent signal interference from cell clustering.

MSC transplantation

The in vivo experiments utilized wild-type C57BL/6 mice and 10-month-old APPswe/PS1dE9 double transgenic mice, which were based on a C57BL/6 genetic background and expressed a chimeric mouse/human APP with the Swedish mutation (KM670/671NL), along with human presenilin 1 featuring the deltaE9 mutation. A total of 5 µL MSCs and eMSCs (5×10^5 cells μL^{-1}) pretreated with $APOs@BP_{miR\text{-}124}$, $APOs@^{atRAN}BP_{miR\text{-}NC}$, $APOs@^{atRAN}NP_{miR\text{-}124}$, $APOs@^{atRAN}BP_{miR\text{-}124}$ (equivalent dosage of miR-124 at 100 nM and atRAN at 1 mM), respectively, were bilaterally injected into the hippocampus (2.5 µL per side) at a rate of 0.5 $\mu L\ min^{-1}$. The injection site coordinates were relative to bregma: anteroposterior, -2.00 mm; mediolateral, 1.50 mm; and dorsoventral, -2.00 mm. The entire injection process was meticulously controlled by the programmed settings of the stereotaxic injection pump and mouse stereotaxic instrument (Shanghai Yuyan Instruments Co., Ltd). The needle was left for 5 min to avoid cell suspension overflow during needle withdrawal. The wound was closed aseptically and disinfected. Mice were housed in individually ventilated cages with attention to postoperative heat retention, provided with a standard diet, and allowed free access to water at a temperature of 23 °C and 45-55% relative humidity.

Statistical analysis

For quantitative analysis, a minimum of three replicates were analyzed. All results were expressed as mean ± SD unless otherwise indicated. Statistical significance of differences was analyzed by GraphPad Prism 8.0.2. Statistical tests utilized for each experiment were specified in the legends of figures, and statistical significance was defined as $P < 0.05$.

Reporting summary

Further information on research design is available in the Nature Portfolio Reporting Summary linked to this article.

Data availability

The main data supporting the results of this study are available within the paper and its Supplementary Information. The transcriptomic data generated in this study have been deposited in NCBI Sequence Read Archive database under accession no. PRJNA1089125. All data generated in this study are provided in the Source Data file. Source data is available for Figs. 2b, c, e, f, h–j, 3a-d, f–h, j, l, 4a, b, e, 5d, g, i, 6b, e, and g and Supplementary Figs. 4b, 8, 9, 10, 11, 12, 13, 14, 21, 22 and 24 in the associated source data file. Source data are provided with this paper.

References

1. De Luca, M. et al. Advances in stem cell research and therapeutic development. *Nat. Cell Biol.* **21**, 801–811 (2019).
2. Levy, O. et al. Shattering barriers toward clinically meaningful MSC therapies. *Sci. Adv.* **6**, eaba6884 (2020).
3. Liu, L., Michowski, W., Kolodziejczyk, A. & Sicinski, P. The cell cycle in stem cell proliferation, pluripotency and differentiation. *Nat. Cell Biol.* **21**, 1060–1067 (2019).
4. Duester, G. Retinoic acid synthesis and signaling during early organogenesis. *Cell* **134**, 921–931 (2008).
5. Zhang, R. et al. Traceable nanoparticle delivery of small interfering rna and retinoic acid with temporally release ability to control neural stem cell differentiation for Alzheimer's Disease Therapy. *Adv. Mater.* **28**, 6345–6352 (2016).
6. Huang, D. et al. A nanoformulation-mediated multifunctional stem cell therapy with improved beta-amyloid clearance and neural regeneration for alzheimer's disease. *Adv. Mater.* **33**, e2006357 (2021).
7. Brennan, G. P. & Henshall, D. C. MicroRNAs as regulators of brain function and targets for treatment of epilepsy. *Nat. Rev. Neurol.* **16**, 506–519 (2020).
8. Cates, K. et al. Deconstructing stepwise fate conversion of human fibroblasts to neurons by microRNAs. *Cell Stem Cell* **28**, 127–140.e129 (2021).
9. Stewart, M. P. et al. In vitro and ex vivo strategies for intracellular delivery. *Nature* **538**, 183–192 (2016).
10. Kimbrel, E. A. & Lanza, R. Next-generation stem cells - ushering in a new era of cell-based therapies. *Nat. Rev. Drug Discov.* **19**, 463–479 (2020).
11. Stewart, M. P., Langer, R. & Jensen, K. F. Intracellular delivery by membrane disruption: mechanisms, strategies, and concepts. *Chem. Rev.* **118**, 7409–7531 (2018).
12. Liu, H. et al. Nanoassemblies with effective serum tolerance capability achieving robust gene silencing efficacy for breast cancer gene therapy. *Adv. Mater.* **33**, e2003523 (2021).
13. Mahmoudi, M., Landry, M. P., Moore, A. & Coreas, R. The protein corona from nanomedicine to environmental science. *Nat. Rev. Mater.* **8**, 422–438 (2023).
14. Ren, J. et al. Chemical and biophysical signatures of the protein corona in nanomedicine. *J. Am. Chem. Soc.* **144**, 9184–9205 (2022).
15. Wheeler, K. E. et al. Environmental dimensions of the protein corona. *Nat. Nanotechnol.* **16**, 617–629 (2021).
16. Li, M. et al. Nanoparticle elasticity affects systemic circulation lifetime by modulating adsorption of apolipoprotein A-I in corona formation. *Nat. Commun.* **13**, 4137 (2022).
17. Miao, Y. et al. Regulating protein corona on nanovesicles by glycosylated polyhydroxy polymer modification for efficient drug delivery. *Nat. Commun.* **15**, 1159 (2024).
18. Sevugan Chetty, P. et al. Apolipoprotein A-I helical structure and stability in discoidal high-density lipoprotein (HDL) particles by hydrogen exchange and mass spectrometry. *Proc. Natl. Acad. Sci. Usa.* **109**, 11687–11692 (2012).
19. Jin, Y. et al. A nanodisc-paved biobridge facilitates stem cell membrane fusogenicity for intracerebral shuttling and bystander effects. *Adv. Mater.* **35**, e2302367 (2023).
20. Oda, M. N., Forte, T. M., Ryan, R. O. & Voss, J. C. The C-terminal domain of apolipoprotein A-I contains a lipid-sensitive conformational trigger. *Nat. Struct. Biol.* **10**, 455–460 (2003).
21. Wang, R. et al. Phenylboronic acid modification augments the lysosome escape and antitumor efficacy of a cylindrical polymer brush-based prodrug. *J. Am. Chem. Soc.* **143**, 20927–20938 (2021).
22. Cho, Y. W. et al. Single metal-organic framework-embedded nanopit arrays: A new way to control neural stem cell differentiation. *Sci. Adv.* **8**, eabj7736 (2022).
23. Lu, Y. L., Liu, Y., McCoy, M. J. & Yoo, A. S. MiR-124 synergism with ELAVL3 enhances target gene expression to promote neuronal maturity. *Proc. Natl. Acad. Sci. USA.* **118**, (2021).
24. Ferreira, R., Napoli, J., Enver, T., Bernardino, L. & Ferreira, L. Advances and challenges in retinoid delivery systems in regenerative and therapeutic medicine. *Nat. Commun.* **11**, 4265 (2020).
25. Xiong, M. et al. Human stem cell-derived neurons repair circuits and restore neural function. *Cell Stem Cell* **28**, 112–126.e116 (2021).
26. Jin, Y. Created in BioRender. https://BioRender.com/m97k839 (2025).
27. Jin, Y. Created in BioRender. https://BioRender.com/i41e942 (2025).
28. Jin, Y. Created in BioRender. https://BioRender.com/m61k697 (2025).
29. Jin, Y. Created in BioRender. https://BioRender.com/i81x173 (2025).
30. Jin, Y. Created in BioRender. https://BioRender.com/b21r008 (2025).
31. Jin, Y. Created in BioRender. https://BioRender.com/l88s832 (2025).

Acknowledgements

This work is financially supported by the National Natural Science Foundation of China (82372113 received by Y.D., 82104097 received by H.Z., and 82373815 received by J.Z.), the National Ten Thousand Talents Program for Young Top-notch Talents, and Natural Science Foundation of Jiangsu Province (BK20210426, received by Y.D.). In addition, we thank Natural Science Foundation for Distinguished Young Scholars of Jiangsu Province (BK20240096, received by Y.D.), Jiangsu 333 High-level Talent Training Project ([2022] 3-16-190, received by Y.D.), Double First-Rate Construction Plan of China Pharmaceutical University (CPU2022QZ18, received by J.Z.), and Fundamental Research Funds for the Central Universities (2632023TD05, received by H.Z). We thank the Cellular and Molecular Biology Center of China Pharmaceutical University for assistance with CLSM.

Author contributions

J.Z., H.Z., and Y.D. conceived and supervised the project. Y.J. and G.H. performed experiments, analyzed and interpreted data. Y.G. and H.C. helped with cellular and animal experiments. C.S. and J.N. participated in experimental design and data analysis. Y.J. wrote the manuscript. Y.D. edited the manuscript and provided suggestions. All the authors discussed the results and commented on the manuscript.

Competing interests

The authors declare no competing interests.

Additional information

Supplementary information The online version contains supplementary material available at https://doi.org/10.1038/s41467-025-57278-8.

Correspondence and requests for materials should be addressed to Jianping Zhou, Huaqing Zhang or Yang Ding.

Peer review information *Nature Communications* thanks Liming Bian and Kiminobu Sugaya for their contribution to the peer review of this work. A peer review file is available.

Reprints and permissions information is available at http://www.nature.com/reprints

Publisher's note Springer Nature remains neutral with regard to jurisdictional claims in published maps and institutional affiliations.

Open Access This article is licensed under a Creative Commons Attribution-NonCommercial-NoDerivatives 4.0 International License, which permits any non-commercial use, sharing, distribution and reproduction in any medium or format, as long as you give appropriate credit to the original author(s) and the source, provide a link to the Creative Commons licence, and indicate if you modified the licensed material. You do not have permission under this licence to share adapted material derived from this article or parts of it. The images or other third party material in this article are included in the article's Creative Commons licence, unless indicated otherwise in a credit line to the material. If material is not included in the article's Creative Commons licence and your intended use is not permitted by statutory regulation or exceeds the permitted use, you will need to obtain permission directly from the copyright holder. To view a copy of this licence, visit http://creativecommons.org/licenses/by-nc-nd/4.0/.

© The Author(s) 2025